# Lattice Breathing Inhibited Layered Vanadium Oxide Ultrathin Nanobelts for Enhanced Sodium Storage

Qiulong Wei,[†,‡] Zhouyang Jiang,[†,§] Shuangshuang Tan,[‡] Qidong Li,[‡] Lei Huang,[‡] Mengyu Yan,[‡] Liang Zhou,*[,‡] Qinyou An,[‡] and Liqiang Mai*[,‡]

[‡]State Key Laboratory of Advanced Technology for Materials Synthesis and Processing and [§]School of Chemistry, Chemical Engineering and Life Science, Wuhan University of Technology, Wuhan 430070, P. R. China

S *Supporting Information*
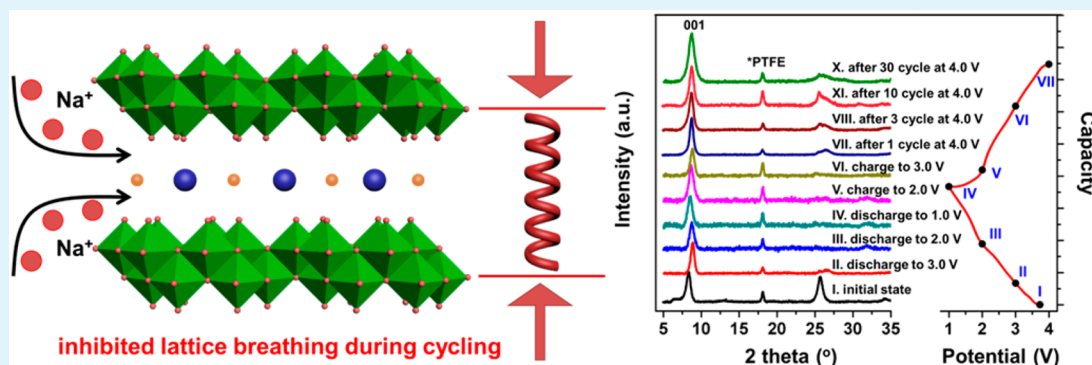
ABSTRACT: Operating as the "rocking-chair" battery, sodium ion battery (SIB) with acceptable high capacity is a very promising energy storage technology. Layered vanadium oxide xerogel exhibits high sodium storage capacity. But it undergoes large lattice breathing during sodiation/desodiation, resulting in fast capacity fading. Herein, we develop a facile hydrothermal method to synthesize iron preintercalated vanadium oxide ultrathin nanobelts (Fe-VO$_x$) with constricted interlayer spacing. Using the Fe-VO$_x$ as cathode for SIB, the lattice breathing during sodiation/desodiation is largely inhibited and the interlayer spacing is stabilized for reversible and rapid Na$^+$ insertion/extraction, displaying enhanced cycling and rate performance. This work presents a new strategy to reduce the lattice breathing of layered materials for enhanced sodium storage through interlayer spacing engineering.

KEYWORDS: sodium ion battery, vanadium oxide, layered structure, nanobelt, lattice breathing

To take full advantages of the renewable energy, the development of large-scale energy storage systems (ESSs) that balance electricity generations and demand is extremely important.[1–3] The rechargeable battery is one of the most promising energy storage technologies.[1,3–5] Lithium-ion batteries (LIBs) with high capacity and high energy conversion efficiency have been widely investigated in the past decades. They are now being developed as green power sources for electric vehicles (EVs) and large-scale ESSs. However, the huge requirements of lithium may bring an increasing in cost due to its low abundance on the earth.[1] Therefore, an abundant, nontoxic, stable, and cheap substitution is indeed needed to satisfy the increasing requirements. Sodium, which has similar physicochemical properties to lithium, is an abundant and low-cost element.[1,2,4,6–8] Operating as the "rocking-chair" battery, sodium ion battery (SIB) with acceptable high capacity is a very reasonable alternative, especially for large-scale ESSs.[2,8] However, the radius of Na$^+$ is 1.43 times to that of Li$^+$ (97 vs 68 pm), resulting in sluggish electrochemical reaction kinetics.[2,6,7] Thus, host materials with large diffusion channels are required for the reversible and rapid Na$^+$ insertion and extraction.[9]

Layered transition metal compounds have been extensively studied as ion insertion hosts for electrochemical energy storage.[6,10] Among them, layered vanadium oxides with high theoretical capacity and large abundance have been extensively investigated in LIBs and supercapacitors.[11–15] Constructed by [VO$_6$] octahedra and/or [VO$_5$] square pyramid with long V–O bond and short vanadyl bond V═O, various vanadium oxide layered structures, including the V$_2$O$_5$, V$_6$O$_{13}$, VO$_2$(B), VO$_2$(A) and so forth, are formed and exhibit promising lithium/sodium storage performance.[15–17] The orthorhombic V$_2$O$_5$, consisting of [VO$_5$] square pyramids with an interlayer spacing of ~4.37 Å, exhibits reversible Li$^+$ insertion/extraction behavior. However, it is generally not suitable for long-term reversible Na$^+$ insertion/extraction.[18,19] To improve the sodium storage performance of layered materials, efforts have been focusing on
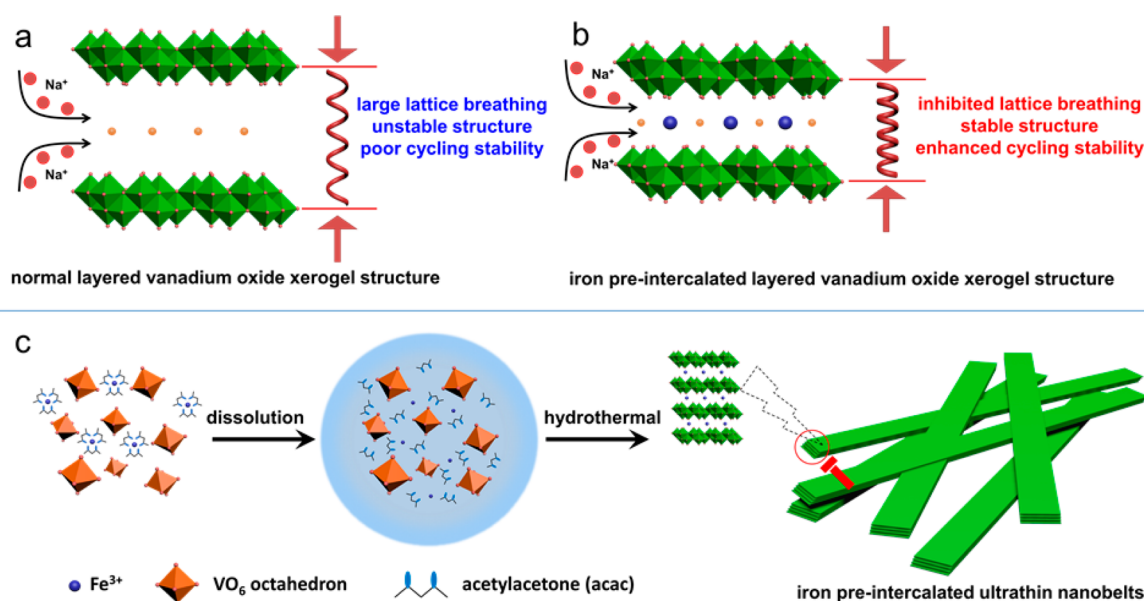
Figure 1. Schematic illustration of the layered vanadium oxide xerogel structure. (a) Normal vanadium oxide xerogel structure with large lattice breathing during sodiation/desodiation shows unstable structure and poor cycling stability. (b) Iron preintercalated vanadium oxide xerogel with inhibited lattice breathing during sodiation/desodiation displays enhanced structural stability and cycling performance. (c) Schematic formation process of the iron preintercalated vanadium oxide xerogel ultrathin nanobelts.

expanding the interlayer spacing.[19−21] The vanadium oxide xerogel structure is made up of V_2O_5 bilayers, in which all the apexes (vanadyl bonds) are up in one sublayer and down in the other sublayer (Figure 1a).[11,16,22] With a larger interlayer spacing than the orthorhombic V_2O_5, the layered vanadium oxide xerogel structure exhibits remarkable sodium storage capacity.[18,23] During sodiation/desodiation, the xerogel bilayer structure undergoes large lattice parameter changes: the lattice parameter c shrinks during ion insertion and expands during ion extraction.[18] This type of repeated lattice/interlayer shrinkage and expansion, which is like the breath, is termed "lattice breathing". The large lattice breathing leads to the collapse of layered structure, which further results in the deactivation of electrode material and fast capacity fading (Figure 1a).[18,24,25] Therefore, an effective approach is urgently required to solve this issue.

Different from most previous reports focusing on expanding the interlayer spacing of layered materials, in this work, we present that the iron preintercalated vanadium oxide xerogel with constricted interlayer spacing can inhibit the lattice breathing during sodiation/desodiation and enhance the sodium storage performance. A facile hydrothermal method is developed to introduce foreign metal ions into the layered vanadium oxide xerogel. The preintercalated metal ions show strong interactions toward the V_2O_5 bilayers, leading to constricted interlayer spacing (Figure 1b). For Na^+ insertion/extraction, the lattice breathing of the host material is largely inhibited. In addition, the preintercalated ions strengthen the layered structure, enhancing the cycling stability.[24−26]

The iron preintercalated vanadium oxide xerogel nanobelts (Fe-VO_x) are synthesized by using iron(III) acetylacetonate (Fe(acac)$_3$) and V_2O_5 sol as the reactants (Figure 1c). The Fe(acac)$_3$ dissolves and ionizes in water, forming Fe^{3+} and acac$^−$. The organic functional group (acac$^−$) acts as the surfactant for the formation of ultrathin nanobelts. Simultaneously, the iron ions intercalate into the layers during the hydrothermal process. It is expected that the as-synthesized ultrathin nanobelts may provide largely shortened ion diffusion length and continuous electrons transport, benefiting for the sodium storage.

The as-prepared samples are first characterized by X-ray diffraction (XRD). The XRD patterns of both pristine vanadium oxide xerogel nanobelts (VO_x) and Fe-VO_x (Figure 2a) show typical (00l) diffraction peaks, which are characteristic for vanadium oxide xerogel structure (JCPDF No. 40−1296).[11,18,27] It should be noted that the (001) peak of the Fe-VO_x is shifted to high angle compared to that of VO_x, indicating the constriction along c-axis after iron preintercalation. From the position of the (001) peak, the spacing between adjacent layers is calculated to be 14.0 and 10.6 Å for the VO_x and Fe-VO_x, respectively. The thermogravimetry analysis (TGA) results of Fe-VO_x and VO_x (Figure S1) exhibit the same weight loss, indicating that the intercalated iron ions have no influence on the crystal water content. Thus, the constriction of the interlayer spacing is mainly caused by the preintercalation of iron ions.[28]

The samples are further characterized by Raman, Fourier transform infrared (FTIR) spectra, and X-ray photoelectron spectroscopy (XPS), as shown in Figure S2 and Figure 2b. Generally, both samples display similar Raman spectra (Figure S2a). The strong low-wavenumber peak at 138 cm^{-1} is attributed to the skeleton bent vibration, which is characteristic for vanadium oxide layered structures.[13,19] The peaks at 190, 280, 402, and 685 cm^{-1} are originated from the bending and stretching vibrations of the V−O bond, while the peak at 991 cm^{-1} is associated with the V=O stretching vibrations.[19] This structure is also verified by the FTIR spectra (Figure S2b), in which the peaks centered at 525 and 764 cm^{-1} are assigned to the V−O−V stretching modes and the peak at 998 cm^{-1} is attributed to the V=O stretching. The position of the V=O stretching is related to the valence state of the vanadium. Compared to previous literatures, the slight red shift of the stretching band of V=O indicates the partial reduction of V^{5+} to V^{4+} in the samples.[18] The XPS is further carried out to
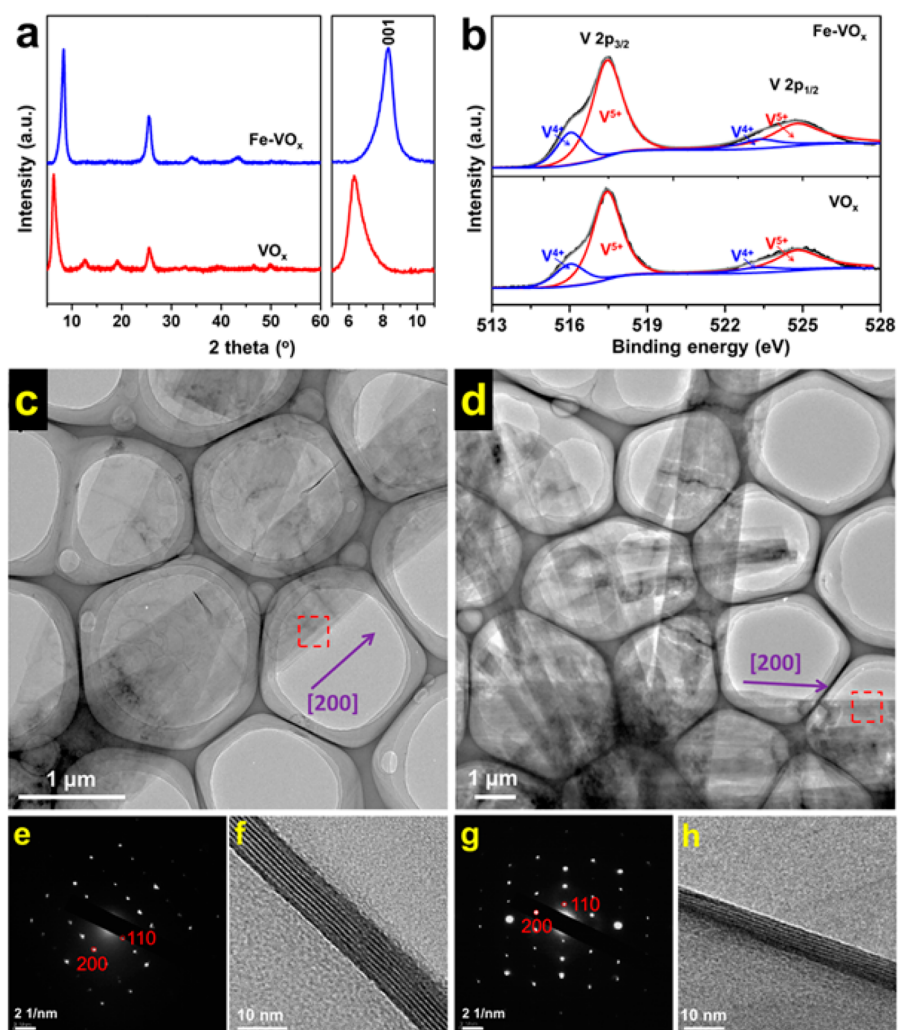
Figure 2. (a) XRD patterns and (b) XPS spectrum of V2P binding energy region of the Fe-VO$_x$ and VO$_x$. TEM images of the (c) VO$_x$ and (d) Fe-VO$_x$ ultrathin nanobelts. (e) SAED pattern of the VO$_x$ nanobelt, selected region in c. (f) Side-view HRTEM of a curled VO$_x$ nanobelt edge. (g) SAED pattern of Fe-VO$_x$ nanobelt, selected region in d. (h) Side-view HRTEM of a curled Fe-VO$_x$ nanobelt edge.

identify the chemical composition of the as-prepared samples (Figure 2b). The deconvoluted V $2p_{3/2}$ binding energies of 517.4 and 516.0 eV are consistent with the typically reported values for V^{5+} and V^{4+}. The V^{4+}/V^{5+} ratio is determined to be 20.0 and 22.5% for VO$_x$ and Fe-VO$_x$, respectively. The XPS spectrum of Fe 2p indicates a partial reduction of Fe^{3+} to Fe^{2+} during the synthesis process (Figure S3). The partial reduction of Fe^{3+} and V^{5+} to Fe^{2+} and V^{4+} is caused by the existence of organic species acac$^-$, which acts as a reducing agent during the hydrothermal condition. Additionally, the inductively coupled plasma (ICP) analysis figures out the atomic ratio of Fe/V is 0.056/1 (Table S1).

The morphologies of the samples are investigated by scanning electronic microscopy (SEM) and transmission electronic microscopy (TEM), as shown in Figure S4 and Figure 2c−h. Both the VO$_x$ and Fe-VO$_x$ are composed of ultrathin nanobelts (Figure 2c, d and Figure S4). The selected area electron diffraction (SAED) patterns of the VO$_x$ and Fe-VO$_x$ nanobelts are shown in Figure 2e and 2g, respectively. Both patterns exhibit the same inner-layer lattice structure which can be indexed to the [001] zone axis. The growth direction of the nanobelts is [200] direction. Due to the ultrathin nature, the nanobelts may curl at the edge, from where

the layered structure of the nanobelts can be clearly discerned and the thickness is determined to be below 10 nm (Figure 2f, h). The energy-dispersive X-ray spectroscopy (EDS) result confirms that the existence of Fe in the Fe-VO$_x$ nanobelt (Figure S5). Combining the above results together, it is concluded that the iron ions indeed intercalate into the layers and the preintercalated ions only constrict the interlayer spacing rather than destroy the layered structure.

Time-dependent experiments are carried out to understand the formation process of the ultrathin nanobelts. It is found that the hydrothermal reaction time plays a key role in the formation of nanobelts. The nanobelts begin to form after 12 h reaction, but the yield is low (Figures S6 and S7). Extending the reaction time leads to the formation of more nanobelts. After 48 h, the supernatant become colorless and transparent, indicating the low concentration of vanadium species in solution and the almost completed reaction. From the XRD patterns of the products (Figure S7a), it is noted that the (001) diffraction does not vary in position with reaction time, suggesting the simultaneous nanobelts formation and iron intercalation. In addition, with the increasing ratios of Fe(acac)$_3$: V$_2$O$_5$ sols, the iron species tends to self-aggregate, resulting in the nanoparticles on the nanobelts (Figure S8).
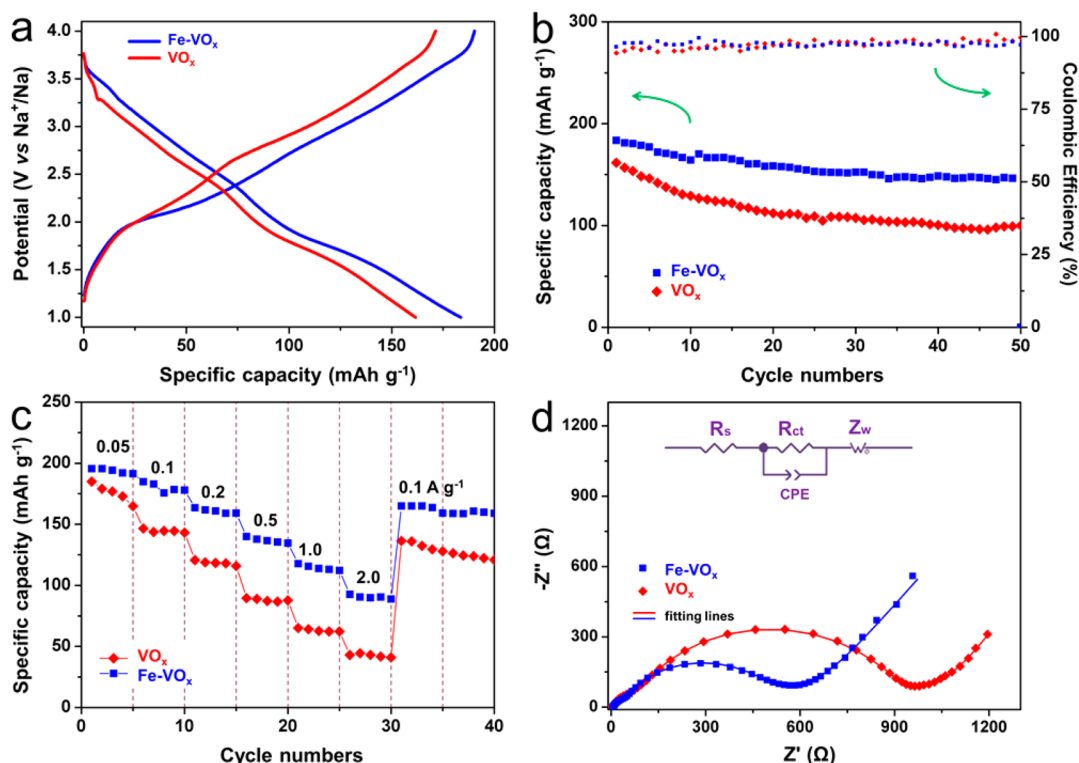
Figure 3. (a) Charge−discharge curves and (b) cycling performance of the Fe-VO$_x$ and VO$_x$ at a current density of 0.1 A g^{-1}. (c) Rate performance and (d) Nyquist plots of the Fe-VO$_x$ and VO$_x$.

The XRD patterns (Figure S8d) indicate almost the same interlayer spacing of Fe-VO$_x$ but with some impurity phase. The ion self-intercalation method we developed is a general strategy. It can be generalized to the synthesis of other metal ions preintercalated VO$_x$ nanobelts, such as Ca, Mo, and Zn preintercalated VO$_x$ nanobelts, as shown in Figure S9.

Electrochemical properties of the samples are investigated by assembling the coin cells (2016-type) with metallic sodium as the anode. Figure 3a shows the discharge and charge curves at the current density of 0.1 A g^{-1} in 1.0−4.0 V. Both VO$_x$ and Fe-VO$_x$ exhibit a short discharge plateau at around 1.70 V. Cyclic voltammetry (CV) curves (Figure S10) display the clear cathodic peaks at ∼1.70 V and anodic peaks at ∼2.20 V for both VO$_x$ and Fe-VO$_x$. The peak current and surrounded area of the Fe-VO$_x$ are larger than those of the VO$_x$, indicating faster kinetics during electrochemical reaction and higher capacity of the Fe-VO$_x$. The initial discharge capacity of the VO$_x$ and Fe-VO$_x$ is 161 and 184 mAh g^{-1} at 0.1 A g^{-1}, respectively. The cycling performances of the samples are shown in Figure 3b. Overall, the Fe-VO$_x$ displays a more stable cycling performance than VO$_x$. The capacity retention of Fe-VO$_x$ after 50 cycles is 80.0%, higher than that of the VO$_x$ (62.1%). The rate capability is further evaluated by cycling at various current densities ranging from 0.05 to 2.0 A g^{-1}. The Fe-VO$_x$ cathode delivers a high capacity of 196 mAh g^{-1} at 0.05 A g^{-1}. High-rate capacities of 118 and 92 mAh g^{-1} are obtained at 1.0 and 2.0 A g^{-1}, respectively. These values are higher than those of the VO$_x$ (65 and 43 mAh g^{-1} at 1.0 and 2.0 A g^{-1}) and comparable to the previous reports.[19,23,28,29] To understand the enhanced electrochemical performance of Fe-VO$_x$, we carried out four-point probe test and electrochemical impedance spectra (EIS). The nanobelts are filtered to prepare free-standing films for the four-point probe test. Compared to the VO$_x$, the conductivity of the

Fe-VO$_x$ is improved for 8.6 times (1.2 vs 0.14 mS cm^{-1}).[30] From the Nyquist plots (Figure 3d), the charge transfer resistance (R_{ct}) of Fe-VO$_x$ is 445 Ω, much lower than that of the VO$_x$ (864 Ω). The increased electronic conductivity and charge transfer ability are responsible for the enhanced rate capability of Fe-VO$_x$.

The ex situ XRD, FTIR, SEM, and TEM are carried out to further investigate the sodium storage behavior (Figure 4). Figure 4a, b shows the ex situ XRD patterns of the Fe-VO$_x$ and VO$_x$ at various states of the first cycle (the voltage profile is displayed on the right side) and charged state of following cycles. The refraction at 18.1° comes from the PTFE binder, and it does not change during cycling. The (001) diffraction shifts visibly during the discharge−charge processes (Figure 4a, b), suggesting the evolution of the interlayer spacing (d_{001}). The d_{001} values at each state are calculated and displayed in Figure 4c, d. Both Fe-VO$_x$ and VO$_x$ undergo lattice breathing along c-axis during cycling. During the discharge process, the d_{001} decreases from state I to II and increases slightly from state II to IV. For the VO$_x$, the initial reduction of d_{001} is as large as 3.85 Å. The large shrinkage of d_{001} is caused by the strong interaction between the positively charged Na$^+$ and V$_2$O$_5$ bilayers. For the Fe-VO$_x$, the contraction along c-axis is significantly inhibited, only 0.66 Å. The slight increase in d_{001} from state II to IV is attributed to the intercalation of more Na$^+$, which expands the interlayer spacing. Accompanying the Na$^+$ intercalation (state I to IV), the V=O stretching vibration continuously shifts toward low wavenumber (Figure 4e), indicating the reduction of vanadium valence state.

The ex situ SEM and TEM images of Fe-VO$_x$ after the initial discharge to 1.0 V are shown in Figure S11 and Figure 4f, g. The nanobelt morphology is maintained for both the Fe-VO$_x$ and VO$_x$ (Figure S11). The layered fringes can be clearly
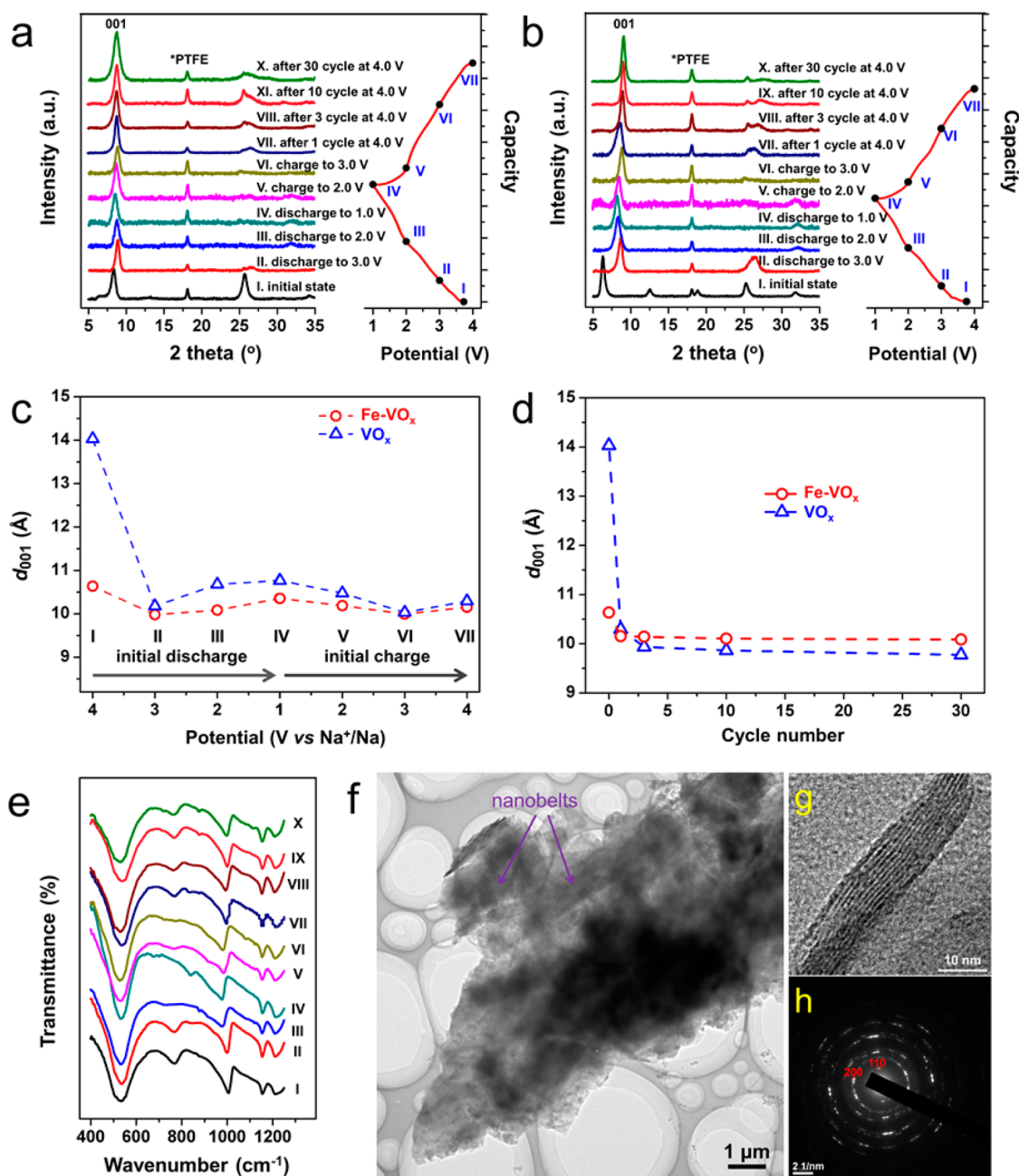
Figure 4. Ex situ XRD patterns of the (a) Fe-VO$_x$ and (b) VO$_x$ collected at various states. (c) d_{001} value variation in the initial discharge−charge cycle. (d) d_{001} variation as a function of cycle number. (e) Ex situ FTIR spectra of the Fe-VO$_x$ collected at various states. (f, g) TEM images and (h) SAED pattern of the Fe-VO$_x$ after the initial discharge to 1.0 V (state IV).

observed in the curled region of the nanobelts (Figure 4g), which is consistent with the ex situ XRD results. The SAED pattern (Figure 4h) shows that the inner layer lattice is still maintained after the Na$^+$ intercalation, which is consistent with the unaffected V−O−V stretching vibration (at 525 cm^{-1}) in the FTIR spectra (Figure 4e). The ICP analysis indicates that the iron content is almost constant during discharging (Table S1). These results unambiguously demonstrate that the Fe-VO$_x$ inner layer is well maintained during charge/discharge, while the interlayer spacing vibrates during Na$^+$ insertion/extraction.

In the following charge process, the interlayer spacing first shrinks (state IV to VI) and then expands (state VI to VII), contrary to the discharge process (Figure 4c). It should be mentioned that the original interlayer spacing cannot be fully

recovered after the initial discharge−charge cycle, especially for VO$_x$. The total shrinkage of the d_{001} for VO$_x$ reaches 3.74 Å, whereas that for Fe-VO$_x$ is only 0.49 Å. The reducing of lattice parameter breathing during cycling would be helpful for enhancing the structural stability and thus the cycle life.[24] The XRD patterns after various cycles are also collected (Figure 4a, b) and the d_{001} versus cycle number are shown in Figure 4d. For Fe-VO$_x$, the d_{001} stabilizes at 10.14 Å after the first cycle, while the d_{001} of VO$_x$ decreases quickly in the first three cycles and then levels off at 9.93 Å. The larger stabilized interlayer spacing of Fe-VO$_x$ is beneficial for ion diffusion and thus sodium storage performance.[20]

In summary, a novel and facile strategy is developed to inhibit the lattice breathing of vanadium oxide xerogel during

sodiation/desodiation through iron preintercalation approach. With the iron preintercalation, the lattice breathing along *c*-axis of VO_x is largely reduced from 3.74 to 0.49 Å. The preintercalation of iron also leads to larger stabilized interlayer spacing for reversible Na^+ insertion/extraction. Benefiting from the inhibited lattice breathing and stabilized interlayer spacing, the Fe-VO_x exhibits enhanced cycling and rate performance. This work presents a new strategy to inhibit the lattice breathing of layered materials for enhanced sodium storage through interlayer spacing engineering. It is expected that this strategy can be further applied to other battery systems, like magnesium ion batteries.

ASSOCIATED CONTENT

Ⓢ Supporting Information

The Supporting Information is available free of charge on the ACS Publications website at DOI: 10.1021/acsami.5b06154.

Detailed experimental section and additional figures (PDF)

AUTHOR INFORMATION

Corresponding Authors

*E-mail: mlq518@whut.edu.cn.
*E-mail: liangzhou@whut.edu.cn.

Author Contributions

[†]Q.L.W. and Z.Y.J. contributed equally. The manuscript was written through contributions of all authors. All authors have given approval to the final version of the manuscript.

Notes

The authors declare no competing financial interest.

ACKNOWLEDGMENTS

REFERENCES

(1) Larcher, D.; Tarascon, J. M. Towards greener and more sustainable batteries for electrical energy storage. *Nat. Chem.* **2015**, *7*, 19−29.

(2) Pan, H.; Hu, Y.-S.; Chen, L. Room-temperature stationary sodium-ion batteries for large-scale electric energy storage. *Energy Environ. Sci.* **2013**, *6*, 2338−2360.

(3) Zhang, Q.; Uchaker, E.; Candelaria, S. L.; Cao, G. Nanomaterials for energy conversion and storage. *Chem. Soc. Rev.* **2013**, *42*, 3127−3171.

(4) Kim, H.; Hong, J.; Park, K. Y.; Kim, H.; Kim, S. W.; Kang, K. Aqueous rechargeable Li and Na ion batteries. *Chem. Rev.* **2014**, *114*, 11788−11827.

(5) (a) An, T.; Wang, Y.; Tang, J.; Wang, Y.; Zhang, L.; Zheng, G. A flexible ligand-based wavy layered metal-organic framework for lithium-ion storage. *J. Colloid Interface Sci.* **2015**, *445*, 320−325. (b) Yang, C.-P.; Yin, Y.-X.; Ye, H.; Jiang, K.-C.; Zhang, J.; Guo, Y.-G. Insight into the effect of boron doping on sulfur/carbon cathode in lithium−sulfur batteries. *ACS Appl. Mater. Interfaces* **2014**, *6*, 8789−8795.

(6) Han, M. H.; Gonzalo, E.; Singh, G.; Rojo, T. A comprehensive review of sodium layered oxides: powerful cathodes for Na-ion batteries. *Energy Environ. Sci.* **2015**, *8*, 81−102.

(7) Yabuuchi, N.; Kubota, K.; Dahbi, M.; Komaba, S. Research development on sodium-ion batteries. *Chem. Rev.* **2014**, *114*, 11636−11682.

(8) Zhou, T.; Pang, W. K.; Zhang, C.; Yang, J.; Chen, Z.; Liu, H. K.; Guo, Z. Enhanced sodium-ion battery performance by structural phase transition from two-dimensional hexagonal-SnS_2 to orthorhombic-SnS. *ACS Nano* **2014**, *8*, 8323−8333.

(9) Lee, H. W.; Wang, R. Y.; Pasta, M.; Woo Lee, S.; Liu, N.; Cui, Y. Manganese hexacyanomanganate open framework as a high-capacity positive electrode material for sodium-ion batteries. *Nat. Commun.* **2014**, *5*, 5280.

(10) (a) Naguib, M.; Gogotsi, Y. Synthesis of two-dimensional materials by selective extraction. *Acc. Chem. Res.* **2014**, *48*, 128−135. (b) Naguib, M.; Mochalin, V. N.; Barsoum, M. W.; Gogotsi, Y. MXenes: a new family of two-dimensional materials. *Adv. Mater.* **2014**, *26*, 992−1005. (c) Lukatskaya, M. R.; Mashtalir, O.; Ren, C. E.; Dall'Agnese, Y.; Rozier, P.; Taberna, P. L.; Naguib, M.; Simon, P.; Barsoum, M. W.; Gogotsi, Y. Cation intercalation and high volumetric capacitance of two-dimensional titanium carbide. *Science* **2013**, *341*, 1502−1505.

(11) Sathiya, M.; Prakash, A. S.; Ramesha, K.; Tarascon, J. M.; Shukla, A. K. V_2O_5-anchored carbon nanotubes for enhanced electrochemical energy storage. *J. Am. Chem. Soc.* **2011**, *133*, 16291−16299.

(12) McNulty, D.; Buckley, D. N.; O'Dwyer, C. Synthesis and electrochemical properties of vanadium oxide materials and structures as Li-ion battery positive electrodes. *J. Power Sources* **2014**, *267*, 831−873.

(13) Zhu, J.; Cao, L.; Wu, Y.; Gong, Y.; Liu, Z.; Hoster, H. E.; Zhang, Y.; Zhang, S.; Yang, S.; Yan, Q.; Ajayan, P. M.; Vajtai, R. Building 3D structures of vanadium pentoxide nanosheets and application as electrodes in supercapacitors. *Nano Lett.* **2013**, *13*, 5408−5413.

(14) Yu, R.; Zhang, C.; Meng, Q.; Chen, Z.; Liu, H.; Guo, Z. Facile synthesis of hierarchical networks composed of highly interconnected V_2O_5 nanosheets assembled on carbon nanotubes and their superior lithium storage properties. *ACS Appl. Mater. Interfaces* **2013**, *5*, 12394−12399.

(15) Dai, L.; Gao, Y.; Cao, C.; Chen, Z.; Luo, H.; Kanehira, M.; Jin, J.; Liu, Y. VO_2 (A) nanostructures with controllable feature sizes and giant aspect ratios: one-step hydrothermal synthesis and lithium-ion battery performance. *RSC Adv.* **2012**, *2*, 5265−5270.

(16) Chernova, N. A.; Roppolo, M.; Dillon, A. C.; Whittingham, M. S. Layered vanadium and molybdenum oxides: batteries and electrochromics. *J. Mater. Chem.* **2009**, *19*, 2526−2552.

(17) (a) Oka, Y.; Yao, T.; Yamamoto, N. Powder X-Ray Crystal Structure of VO_2 (A). *J. Solid State Chem.* **1990**, *86*, 116−124. (b) Wang, C.; Liu, X.; Shao, J.; Xiong, W.; Ma, W.; Zheng, Y. Structural transition and temperature-driven conductivity switching of single crystalline VO_2 (A) nanowires. *RSC Adv.* **2014**, *4*, 64021−64026.

(18) Wei, Q.; Liu, J.; Feng, W.; Sheng, J.; Tian, X.; He, L.; An, Q.; Mai, L. Hydrated vanadium pentoxide with superior sodium storage capacity. *J. Mater. Chem. A* **2015**, *3*, 8070−8075.

(19) Su, D.; Wang, G. Single-crystalline bilayered V_2O_5 nanobelts for high-capacity sodium-ion batteries. *ACS Nano* **2013**, *7*, 11218−11226.

(20) Hu, Z.; Wang, L.; Zhang, K.; Wang, J.; Cheng, F.; Tao, Z.; Chen, J. MoS_2 nanoflowers with expanded interlayers as high-performance anodes for sodium-ion batteries. *Angew. Chem.* **2014**, *126*, 13008−13012.

(21) (a) Cao, Y.; Xiao, L.; Sushko, M. L.; Wang, W.; Schwenzer, B.; Xiao, J.; Nie, Z.; Saraf, L. V.; Yang, Z.; Liu, J. Sodium ion insertion in hollow carbon nanowires for battery applications. *Nano Lett.* **2012**, *12*, 3783−3787. (b) Li, Y.; Liang, Y.; Robles Hernandez, F. C.; Deog Yoo, H.; An, Q.; Yao, Y. Enhancing sodium-ion battery performance with

interlayer-expanded MoS$_2$—PEO nanocomposites. *Nano Energy* **2015**, *15*, 453.

(22) Whittingham, M. S. Lithium batteries and cathode materials. *Chem. Rev.* **2004**, *104*, 4271−4302.

(23) Moretti, A.; Maroni, F.; Osada, I.; Nobili, F.; Passerini, S. V$_2$O$_5$ aerogel as a versatile cathode material for lithium and sodium batteries. *ChemElectroChem* **2015**, *2*, 529−537.

(24) Zhou, Y.-N.; Ma, J.; Hu, E.; Yu, X.; Gu, L.; Nam, K.-W.; Chen, L.; Wang, Z.; Yang, X.-Q. Tuning charge-discharge induced unit cell breathing in layer-structured cathode materials for lithium-ion batteries. *Nat. Commun.* **2014**, *5*, 5381.

(25) Zhao, Y.; Han, C.; Yang, J.; Su, J.; Xu, X.; Li, S.; Xu, L.; Fang, R.; Jiang, H.; Zou, X.; Song, B.; Mai, L.; Zhang, Q. Stable alkali metal ion intercalation compounds as optimized metal oxide nanowire cathodes for lithium batteries. *Nano Lett.* **2015**, *15*, 2180−2185.

(26) Lee, J.; Urban, A.; Li, X.; Su, D.; Hautier, G.; Ceder, G. Unlocking the potential of cation-disordered oxides for rechargeable lithium batteries. *Science* **2014**, *343*, 519−522.

(27) Liu, Q.; Li, Z. F.; Liu, Y.; Zhang, H.; Ren, Y.; Sun, C. J.; Lu, W.; Zhou, Y.; Stanciu, L.; Stach, E. A.; Xie, J. Graphene-modified nanostructured vanadium pentoxide hybrids with extraordinary electrochemical performance for Li-ion batteries. *Nat. Commun.* **2015**, *6*, 6127.

(28) Kim, H.; Kim, R. H.; Lee, S. S.; Kim, Y.; Kim, D. Y.; Park, K. Effects of Ni doping on the initial electrochemical performance of vanadium oxide nanotubes for Na-ion batteries. *ACS Appl. Mater. Interfaces* **2014**, *6*, 11692−11697.

(29) Raju, V.; Rains, J.; Gates, C.; Luo, W.; Wang, X.; Stickle, W. F.; Stucky, G. D.; Ji, X. Superior cathode of sodium-ion batteries: orthorhombic V$_2$O$_5$ nanoparticles generated in nanoporous carbon by ambient hydrolysis deposition. *Nano Lett.* **2014**, *14*, 4119−4124.

(30) (a) Zhou, X.; Wu, G.; Gao, G.; Wang, J.; Yang, H.; Wu, J.; Shen, J.; Zhou, B.; Zhang, Z. Electrochemical performance improvement of vanadium oxide nanotubes as cathode materials for lithium ion batteries through ferric ion exchange technique. *J. Phys. Chem. C* **2012**, *116*, 21685−21692. (b) Tian, X.; Xu, X.; He, L.; Wei, Q.; Yan, M.; Xu, L.; Zhao, Y.; Yang, C.; Mai, L. Ultrathin pre-lithiated V$_6$O$_{13}$ nanosheet cathodes with enhanced electrical transport and cyclability. *J. Power Sources* **2014**, *255*, 235−241.